Electromagnetics, 31:315–336, 2011

ISSN: 0272-6343 print/1532-527X online
DOI: 10.1080/02726343.2011.579760

Taylor & Francis
Taylor & Francis Group

Design, Simulation, and Experimental Study of Far-Field Beam-Forming Techniques Using Conformal Waveguide Arrays

C. CARPENTER,[1] B. P. KUMAR,[1] and G. R. BRANNER[2]

[1]Department of Electrical and Electronic Engineering, California State University, Sacramento, Sacramento, California, USA
[2]Department of Electrical and Computer Engineering, University of California, Davis, Davis, California, USA

Abstract *Phased-array antennas have been employed for decades in numerous applications, such as radar, cellular communications, and satellite systems. Satellite links, for example, may require high-gain microwave beams with overall wide area coverage. Phased-array antennas for such an application can typically control position and beam width of individual sectoral patterns within the coverage region. This article presents an economical alternative in a conformal array antenna of open-ended rectangular waveguides, which can generate either multi-beam or single-beam patterns by switching control to different radiator configurations within the array structure. In the implementation to be presented, the conformal array property is realized by an axial shift of the array elements. This provides additional control over multi-beam coverage area and intensity taper. In this article, four array configurations are presented with experimental and simulated results that are shown to be in close agreement.*

Keywords satellite, antenna arrays, multi-beam patterns, conformal, beam forming

1. Introduction

Phased-array antennas have many important applications, including radar in airport surveillance and missile detection and tracking, as well as applications in personal communication systems and in military and satellite communications (Hansen, 1998). During recent decades, phased-array systems have made significant advances with the development of many major radar systems, such as PATRIOT and communication systems (such as the Boeing common data link [CDL] radio system) and low Profile, Ku band SatCom systems from Loral and RaySat. Due to many recent advances, including monolithic microwave integrated circuits (MMIC), photonics, and digital beam forming, phased-array systems and technology continue to progress rapidly.

This article is based on a phased-array design for applications such as satellite links (Morton & Pasala, 2006; Hopkins et al., 2004; Caille et al., 2002; Godara, 1997), which require high-gain multi-beams that can be steered over a wide area of coverage. Another important application of phased arrays is in the medical field to detect changes in heat

Received 31 August 2009; accepted 8 August 2010.
Address correspondence to B. P. Kumar, Department of Electrical and Electronic Engineering, California State University, Sacramento, 6000 J Street, Sacramento, CA 95819-6019. E-mail: kumarp@ecs.csus.edu

gradients as a noninvasive technique for the early diagnosis of breast cancer (Bocquet et al., 1990; Sterzer, 2002; Valerie et al., 1993). For both communication and medical applications, planar and nonplanar arrays have been widely studied (Miyata, 1996; Sehm et al., 1998; Kumar & Branner, 1994, 2005), and nonplanar arrays have been found to have wide area coverage and low grating lobes. Array technology typically involves the use of expensive phasing networks and electronic control circuits, which have limited lifetime, especially in terrestrial environments (Hopkins et al., 2004; Caille et al., 2002; Godara, 1997). This article presents a simpler, more robust conformal array design that utilizes a multi-mode structure to switch between different beam profiles and, also, conformal shaping to control the beam width and intensity of individual beams.

This array has been designed in the 16-GHz frequency range and has essentially two modes of beam control that can be effected quite easily. Multi-beam or single-beam generation is primarily achieved by switching among different array geometries, which include two linear and two planar conformal configurations. These will be described in Section 2.3. First, the linear configurations deliver multi-beam patterns in one principal plane and single-beam patterns in the orthogonal principal plane, while the planar configurations deliver multi-beam patterns in both principal planes. Second, the beam width of individual beams can be adjusted by the axial movement of a single central element of the array. The latter control results in change of curvature in the array, and hence, convex, concave, and planar geometries have been realized and studied in this work.

2. Design of the Conformal Antenna Array

This section describes key elements of the antenna under study—respectively, antenna array structure, array feed network, and array configurations.

2.1. Antenna Array Structure

The antenna array structure consists of open waveguide elements that are supported by an outer wooden frame, as shown in Figure 1. The array element positions corresponding to the center of each waveguide aperture are listed in Table 1. The supporting wooden frame is designed to hold a maximum of nine waveguide elements in fixed transverse (x-y) positions while allowing axial (z) coordinate adjustments to the array elements.

Table 1
Element positions of conformal array

Element number	x Position (cm)	y Position (cm)	z Position (cm)
1	10.4	0	0.0
2	5.2	−2.5	0.0
3	5.2	2.5	0.0
4	0.0	−5.2	0.0
5	0.0	0.0	Variable
6	0.0	5.2	0.0
7	−5.2	−2.5	0.0
8	−5.2	2.5	0.0
9	−10.4	0.0	0.0

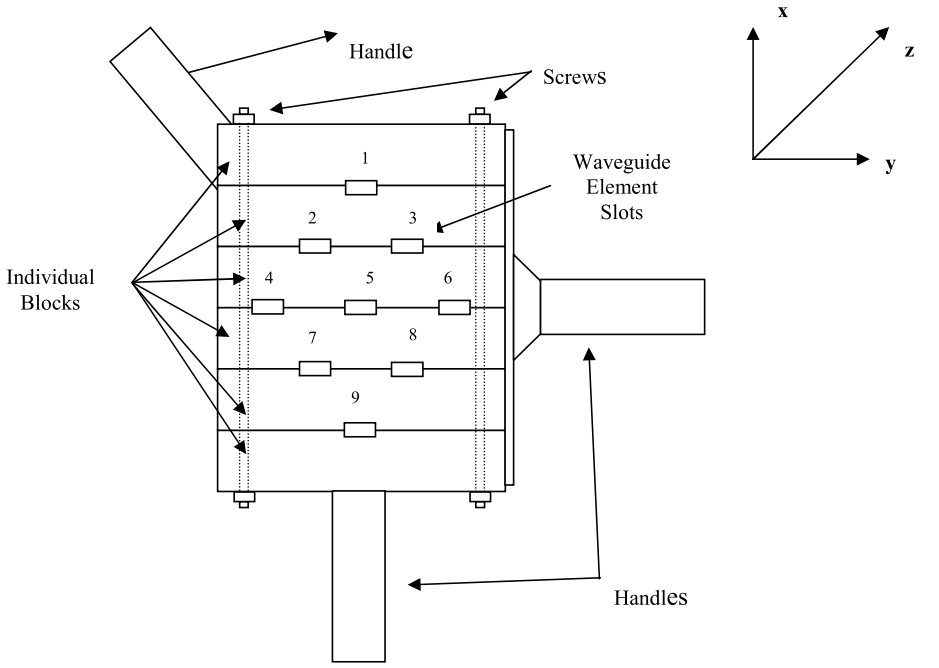

Figure 1. Antenna array structure.

The handles permit positioning of the array in the measurement pedestal for 0°, 90°, or 45° polarizations; however, only 0° and 90° polarizations have been considered in this work. Each waveguide element is 19.5 cm in length with an aperture size of 4 mm × 10.5 mm and copper wall thickness of 1 mm. Using the standard equation (Pozar, 1990), the cutoff frequency for the dominant TE_{10} mode employed here was calculated to be 14.286 GHz, which is well below the operating frequencies utilized in this study.

A number of beam-forming applications were realized by switching among different element combinations. Additionally, axial z-axis shift of the array elements permits control of the beam width; however, such a shift also alters the shape of the array. In this article, three different cases of the central element shift were considered: forward shift (convex surface with negative radius), no shift (planar surface with infinite radius), and backward shift (concave surface with positive radius).

2.2. Array Feed Network

The array feed network is shown in Figures 2(a) and 2(b), which depict the antenna array structure with and without shielding, respectively. Figures 3(a) and 3(b) are schematic diagrams of the array feed network for three-element and five-element array realizations, respectively. As seen in these figures, the feed network is composed of T-junctions, adaptors, and lengths of semi-rigid coaxial cable.

2.3. Array Configurations

In this work, four different array configurations were studied, as illustrated in Figures 4(a)

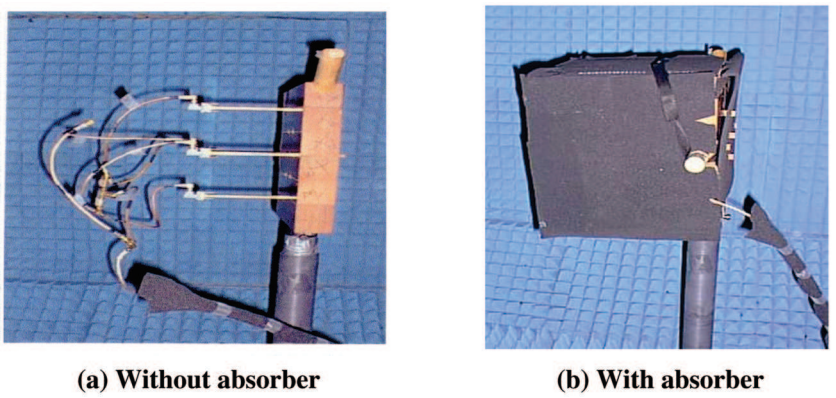

Figure 2. Antenna array structure. (color figure available online)

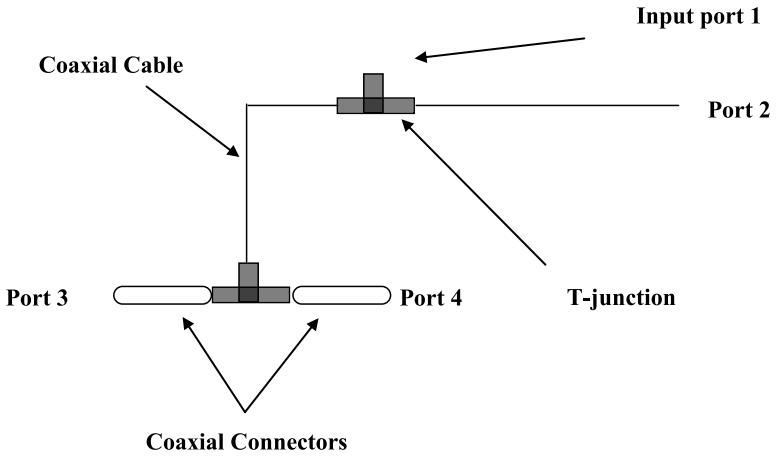

(a)

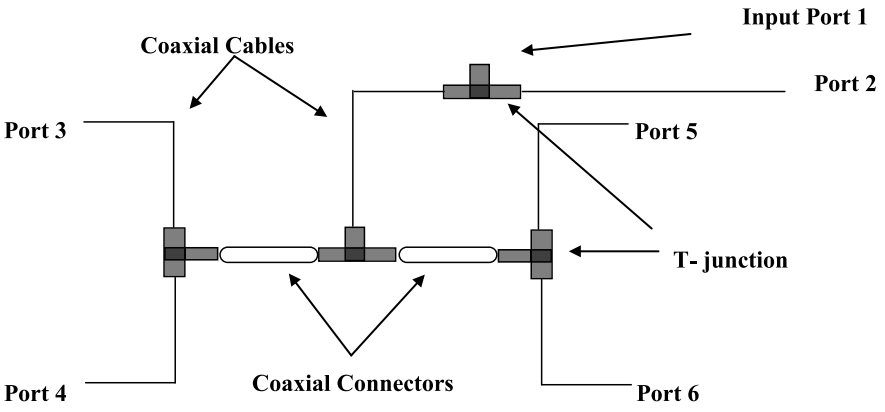

(b)

Figure 3. Schematic of coaxial feed network for: (a) three-element array and (b) five-element array.

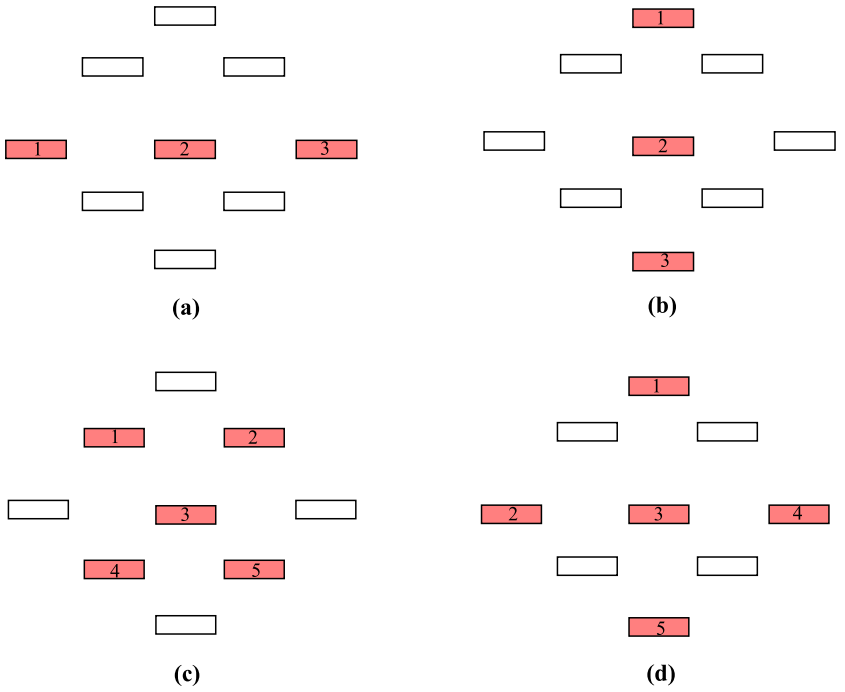

Figure 4. Array configurations under study (shaded pattern shows elements used in array): (a) three-element horizontal, (b) three-element vertical geometry, (c) five-element Close geometry, and (d) five-element Far geometry. (color figure available online)

through 4(d). These are designated as horizontal geometry (Figure 4(a)), vertical geometry (Figure 4(b)), Close geometry (Figure 4(c)), and Far geometry (Figure 4(d)). The respective array realizations are activated by switching power to the elements that are shown shaded in each figure. Figures 4(a) and 4(b) show the *linear* configurations of the array, which primarily deliver a multi-beam in one plane and a single broad beam in the orthogonal plane. Figures 4(c) and 4(d) show the planar configurations of the array, which deliver multi-beams in both planes.

Positive and negative geometries were considered for each of these configurations in order to study the bandwidth control properties of the array. A positive spherical geometry is illustrated in Figure 5(a), with its conformal sphere located in front of the antenna, while the negative spherical geometry is shown in Figure 5(b), with its conformal sphere in the rear of the antenna. The parameter R represents the radius of the conformal sphere, and d_i is the distance of the ith element from the central element, whose position is selected as the reference $(0, 0, 0)$. The axial position of the ith element is determined from the following geometrical considerations, choosing the quadratic solution with smaller curvature:

$$d_i^2 + (R - z_i)^2 = R^2$$

or

$$z_i = R - \sqrt{R^2 - d_i^2}. \tag{1}$$

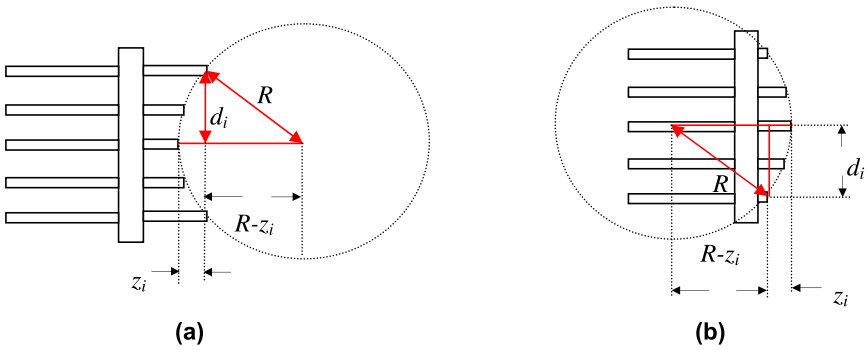

Figure 5. (a) Positive spherical geometry and (b) negative spherical geometry. (color figure available online)

3. Mathematical Modeling of Array

The array mathematical model comprises the following sub-systems: the individual waveguide element pattern, the array factor, and the feed network. The effect that each element has on the overall array pattern can be determined by calculating the array factor. The feed network determines the phase and signal intensity seen by each element in the array and was designed for both uniform phase and intensity. Experiments have shown, however, that the current intensity is not uniform, and this nonuniformity must be accounted for in the mathematical modeling.

3.1. Array Analysis

The mathematical modeling for the individual waveguide element (Figure 6) was developed based on standard array analysis (Hansen, 1998). Note that a and d are the waveguide aperture dimensions, where $d > a$; ϕ is the polarization angle, which is the angle from the x-axis within the x-y-plane; and θ is the scanning angle, which is constrained between $-90°$ and $90°$.

The overall electric field of the array can be written as (Hansen, 1998)

$$E(r) = \frac{e^{-jkr}}{r} f_i(\theta, \phi) \sum_i b_i e^{jk(x_i \sin\theta\cos\phi + y_i \sin\theta\sin\phi + z_i \cos\theta)}, \tag{2}$$

where (x_i, y_i, z_i) represents the center position of the ith array element with excitation b_i, and the function $f_i(\theta, \phi)$ represents the radiation pattern for the ith antenna element.

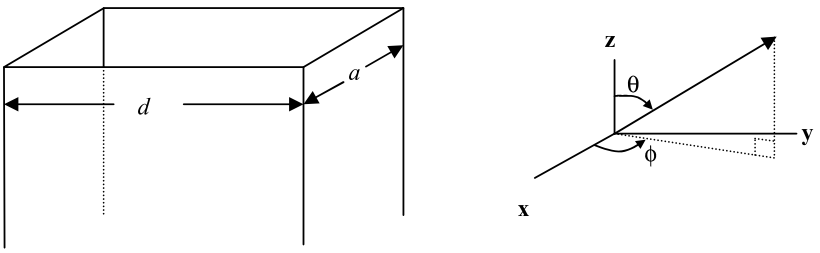

Figure 6. Waveguide element.

In this work, every antenna element is identical; therefore, from Balanis (1997),

$$f_i(\theta, \phi = 0^\circ) = \frac{ab}{\pi\lambda}(1 + \cos\theta)\frac{\sin\left(\frac{\pi a}{\lambda}\sin\theta\right)}{\frac{\pi a}{\lambda}\sin\theta} \tag{3a}$$

and

$$f_i(\theta, \phi = 90^\circ) = \frac{ab}{\pi\lambda}(1 + \cos\theta)\left[\frac{\cos\left(\frac{\pi b}{\lambda}\sin\theta\right)}{\left(\frac{\pi b}{\lambda}\sin\theta\right)^2 - \left(\frac{\pi}{2}\right)^2}\right]. \tag{3b}$$

Substituting Eqs. (3a) and (3b) in Eq. (2), the final mathematical model for the waveguide array system is given in the equations below:

$$E(\theta, \phi = 0^\circ) = \frac{ab}{\pi\lambda}\frac{e^{-jkr}}{r}(1 + \cos\theta)\frac{\sin\left(\frac{\pi a}{\lambda}\sin\theta\right)}{\frac{\pi a}{\lambda}\sin\theta}\sum_i b_i e^{jk(x_i \sin\theta + z_i \cos\theta)} \tag{4a}$$

and

$$E(\theta, \phi = 90^\circ) = \frac{ab}{\pi\lambda}\frac{e^{-jkr}}{r}(1+\cos\theta)\left[\frac{\cos\left(\frac{\pi b}{\lambda}\sin\theta\right)}{\left(\frac{\pi a}{\lambda}\sin\theta\right)^2 - \left(\frac{\pi}{2}\right)^2}\right]\sum_i b_i e^{jk(y_i \sin\theta + z_i \cos\theta)}, \tag{4b}$$

where b_i is the input excitation to the ith radiator.

3.2. Modeling of Array Current Distribution

In order to accurately estimate the array distribution b_i given in Eq. (2), the S-parameter matrix $[S]$ of the complete array feed network was measured. This matrix was measured using an Agilent performance network analyzer (PNA; Agilent Technologies, Santa Rosa, California, USA) for both the three-element and five-element feed networks previously shown in Figures 3(a) and 3(b), respectively. Utilizing this measured data, the array excitation can then be obtained from the following equations:

$$b_i = \sum_{j=1}^{N} S_{ij} a_j, \tag{5a}$$

where

$$a_i = \Gamma_i b_i; \tag{5b}$$

$i = 1$ is the input port, ports $2, \ldots, N$ are the waveguide input ports, Γ_i is the reflection at port i, and assuming $a_1 = 1$.

4. Results and Discussion

The following four subsections detail the theoretical and experimental results for the three-element horizontal array, three-element vertical array, five-element Close array, and the five-element Far array.

4.1. Three-Element Horizontal Linear Array

The schematic of this linear array was previously described in Figure 4(a). Theoretical and measurement studies were made at a frequency of 16.6 GHz for the following conformal geometry radii: $R = 16.75$ cm, $R = \infty$ (planar), and $R = -16.75$ cm. The x-y-z coordinate element positions for this array geometry are given in Table 2.

The measured and theoretical radiation pattern data are given in Figures 7(a) through 7(d) for horizontal array radii of $R = 16.75$ cm, $R = \infty$ (planar geometry), and $R = -16.75$ cm, respectively. Figure 7(a) compares the theoretical and measured gain variation with array radii in the $\phi = 0°$ plane, while Figures 7(b) to 7(d) compare the measured and theoretical radiation field patterns in both principal planes. These figures show quite generally that the beam formation is much more pronounced in the $\phi = 0°$ plane than in the $\phi = 90°$ plane, which has a predominantly flat pattern.

For the $\phi = 0°$ polarization, the measured main lobe 3-dB beam width was found to vary from approximately 3°–5°. In the planar geometry ($R = \infty$) the radiation pattern has a multi-beam structure, which decays gradually and covers a wider scanned range as compared to the spherical geometries of $R = \pm 16.75$ cm. In the latter case, radiation pattern also maintains a multi-beam structure; however, the beam amplitude decays more rapidly on either side of the central beam at 0°.

In the $\phi = 90°$ polarization plane, the radiation pattern has the same form as that of a single element, and both simulated and measured patterns show a single broad beam. The beam width of the radiation pattern is similar in all geometries measured. The only notable difference is the radiation pattern shape. In planar geometries, peaks are seen at approximately $\pm 35°$ and $\pm 60°$, and these peaks become better defined as geometries become more spherical.

The discrepancy between measurement and theory is attributed to the following reasons.

- The theoretical model includes array current compensation, as described in Section 3.2; however, contributions from unaccounted factors, such as diffraction from waveguide edges, would modify the overall array pattern.
- Tolerances in measurement system create some measurement uncertainty, keeping in mind the high frequency of operation (~16 GHz).

4.2. Three-Element Vertical Linear Array

A schematic of this array has presented previously in Figure 4(b), and the x-y-z coordinate element positions for this array geometry are given in Table 3.

Table 2
Position coordinates of three-element horizontal array

Element number	x Position (cm)	y Position (cm)	z Position (cm) for $R = 16.75$ cm	z Position (cm) for planar	z Position (cm) for $R = -16.75$ cm
1	−5.2	0	0	0	0
2	0	0	−0.79	0	0.79
3	5.2	0	0	0	0

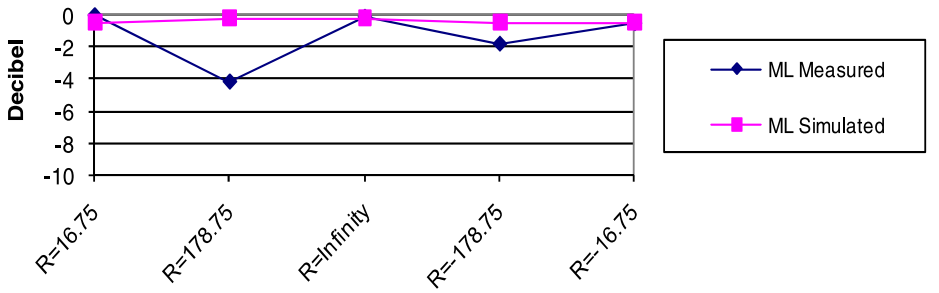

(a)

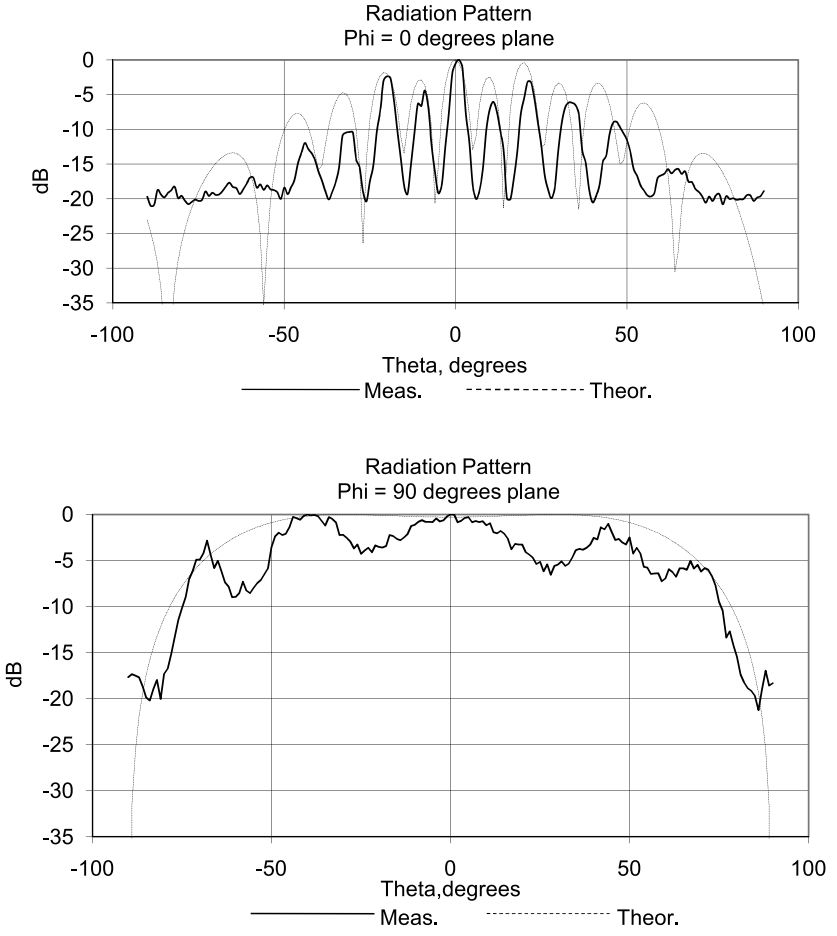

(b)

Figure 7. (a) Main lobe level for three-element horizontal array, (b) radiation patterns of three-element horizontal array ($R = 16.75$ cm), (c) radiation pattern of three-element horizontal array ($R = \infty$), and (d) radiation pattern of three-element horizontal array ($R = -16.75$ cm). (color figure available online) (*continued*)

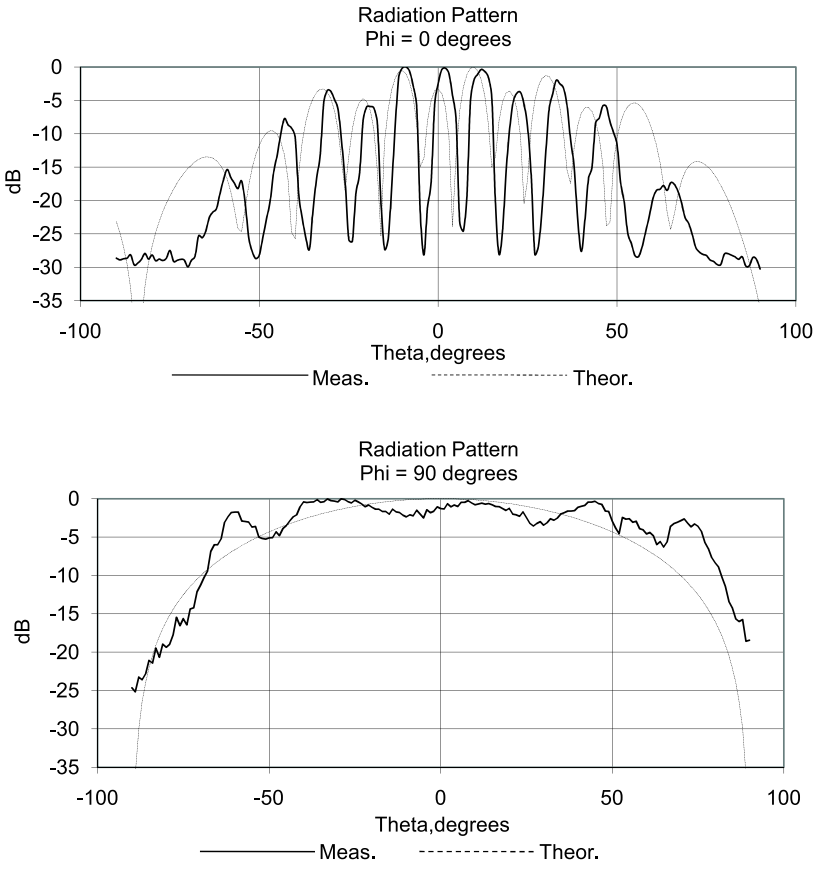

(c)

Figure 7. (*Continued*).

The measured and theoretical radiation pattern data are presented in Figures 8(a) through 8(d) for vertical array radii of $R = 16.75$ cm, $R = \infty$ (planar geometry), and $R = -16.75$ cm, respectively. Figure 8(a) compares the theoretical and measured gain variation for $R = 16.75$ cm, ∞, and -16.75 cm with array radii in the $\phi = 0°$ plane, while Figures 8(b) through 8(d) compare the measured and theoretical radiation field patterns in both principal planes for $R = 16.75$ cm, ∞, and -16.75 cm, respectively.

For the $\phi = 0°$ polarization angle (Figures 8(a)–8(d), upper figure), the measured main lobe 3-dB beam width for the above three geometries was found to vary approximately from 18° –33°, and it can be seen that there is only one lobe at this polarization angle. This results from the fact that the linear array is perpendicular to the scanning plane and, thus, responds similarly to a single element. The measured data shows the radiation pattern is 8° wider for $R = 16.75$ cm and 30° wider for $R = -16.75$ cm.

For the $\phi = 90°$ polarization plane, the separation of the elements in this case has resulted in narrow beam width for all lobes. The measured 3-dB beam width is approximately constant at around 1° for all geometries. However, it is clearly seen that radiation pattern is broader at a planar geometry and more bell shaped or focused for

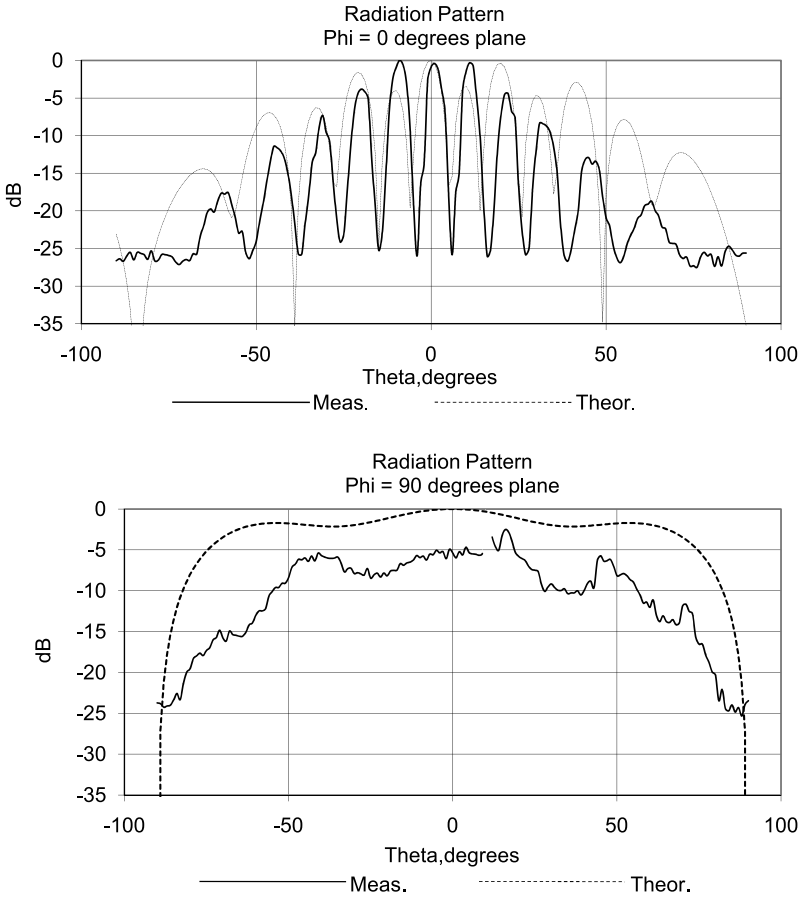

(d)

Figure 7. (*Continued*).

Table 3
Position coordinates of three-element vertical array

Element number	x Position (cm)	y Position (cm)	z Position (cm) for $R = 16.75$ cm	z Position (cm) for planar	z Position (cm) for $R = -16.75$ cm
1	0	−10.4	0	0	0
2	0	0	−3.6	0	3.6
3	0	10.4	0	0	0

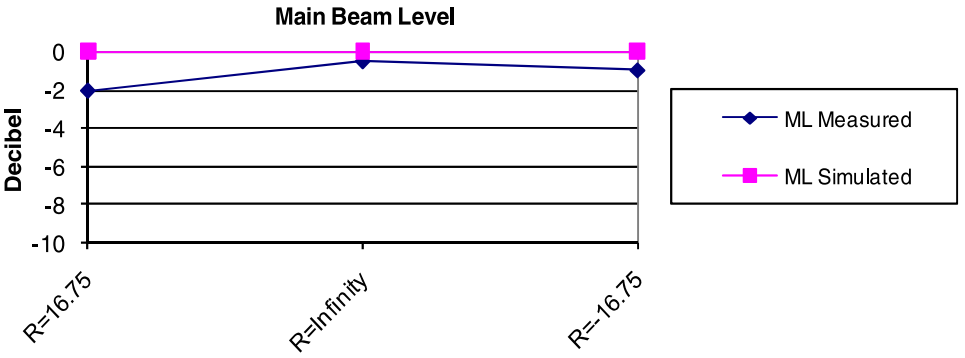

(a)

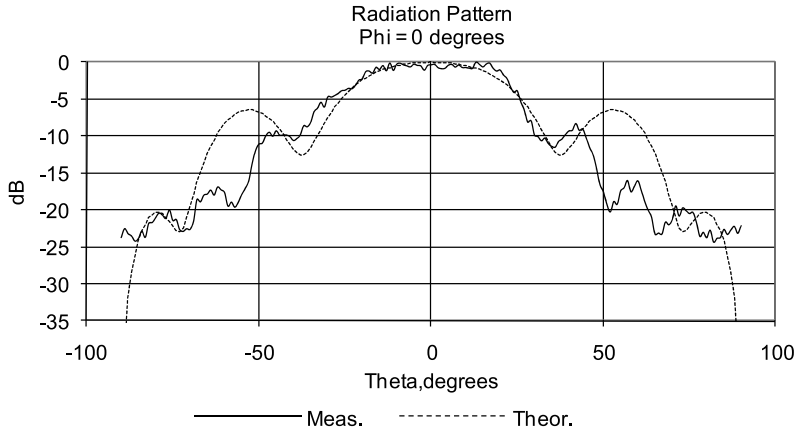

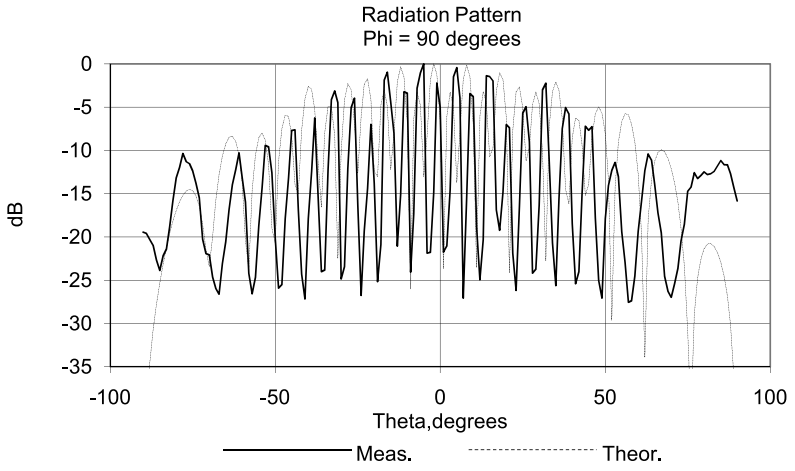

(b)

Figure 8. (a) Main lobe level for three-element vertical array, (b) radiation pattern of three-element vertical array ($R = 16.75$ cm), (c) radiation pattern of three-element vertical array ($R = \infty$), and (d) radiation pattern of three-element vertical array ($R = -16.75$ cm). (color figure available online) (*continued*)

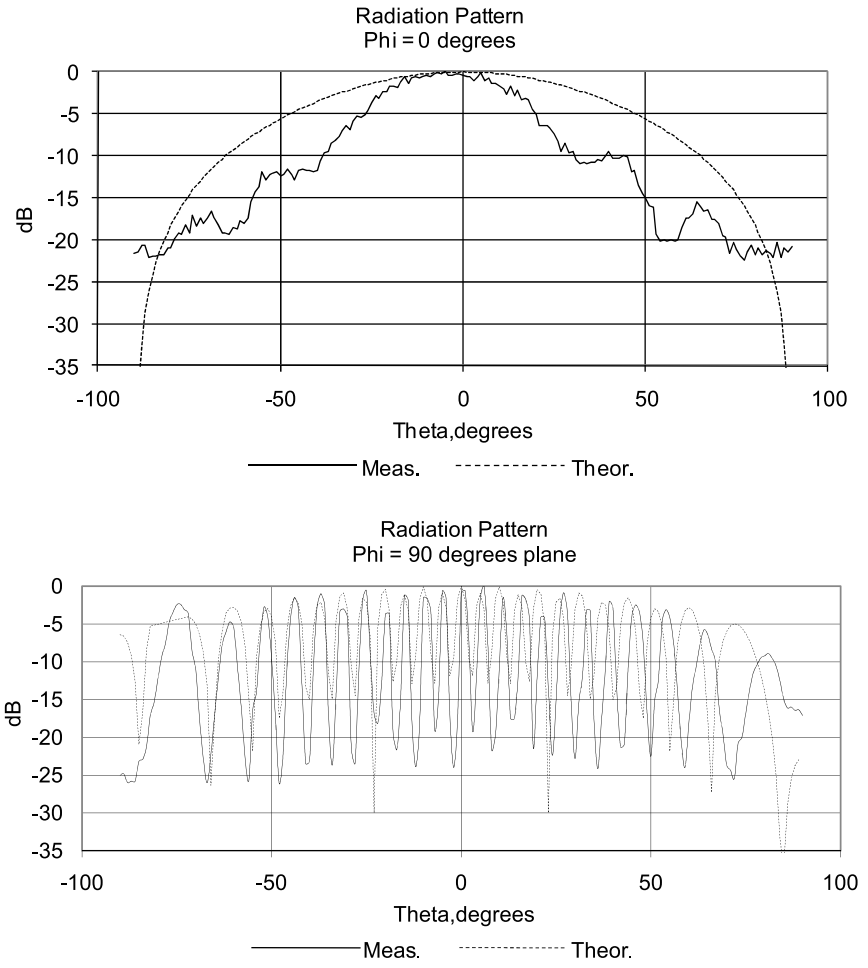

(c)

Figure 8. (*Continued*).

spherical geometries. Positive and negative spherical geometries behave similarly in both measurement and simulation data.

4.3. Five-Element Close Planar Array

This section discusses measurement and simulation data for a five-element Close antenna array (Figure 4(c)) operating at 16.8 GHz. The x-y-z coordinate element positions for this array geometry are given in Table 4 for the different geometries considered for this array.

The measured and theoretical radiation pattern data are presented in Figures 9(a) through 9(d) for Close array radii of $R = 16.75$ cm, $R = \infty$ (planar geometry), and $R = -16.75$ cm, respectively. Figure 9(a) compares the theoretical and measured gain variation with array radii in the $\phi = 0°$ plane, while Figures 9(b) through 9(d) compare the measured and theoretical radiation field patterns in both principal planes.

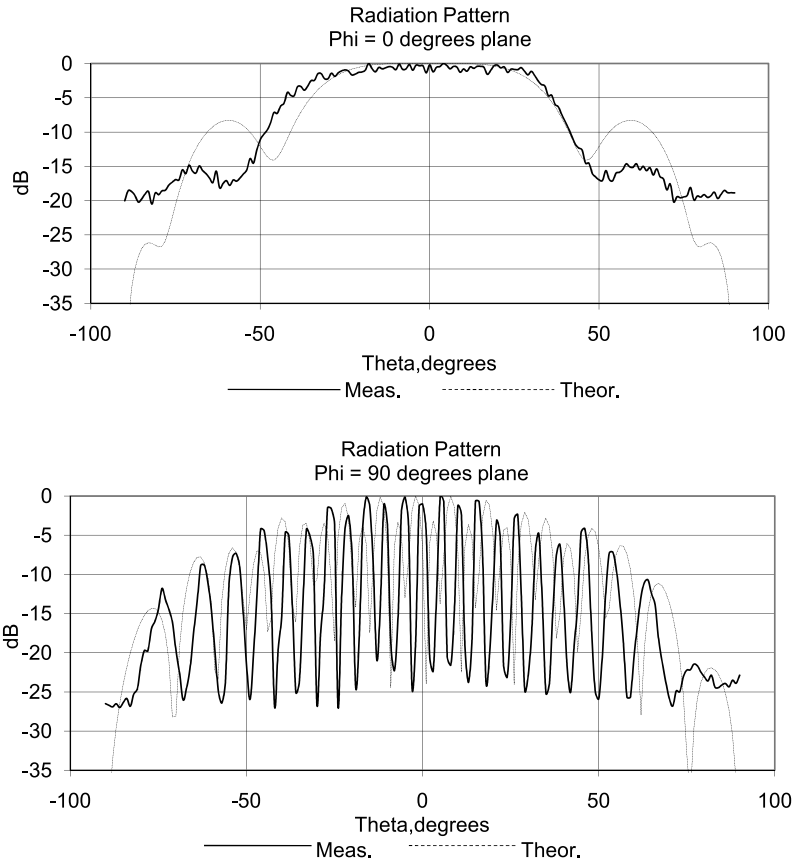

(d)

Figure 8. (*Continued*).

Table 4
Position coordinates of five-element array with Close geometry

Element number	x Position (cm)	y Position (cm)	z Position (cm) for $R = 16.75$ cm	z Position (cm) for planar	z Position (cm) for $R = -16.75$ cm
1	−2.6	5.2	0	0	0
2	2.6	5.2	0	0	0
3	0	0	−1.03	0	1.03
4	−2.6	−5.2	0	0	0
5	2.6	−5.2	0	0	0

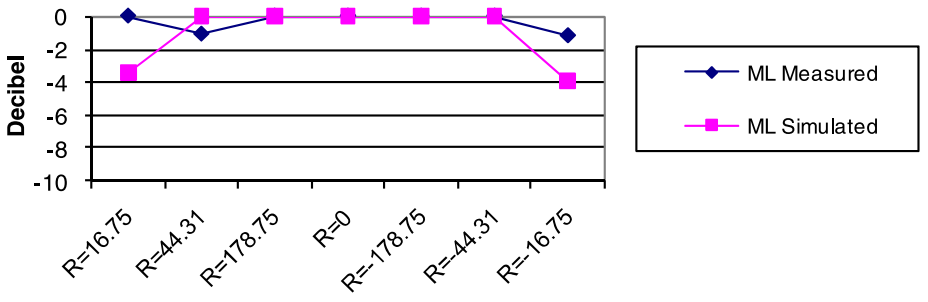

(a)

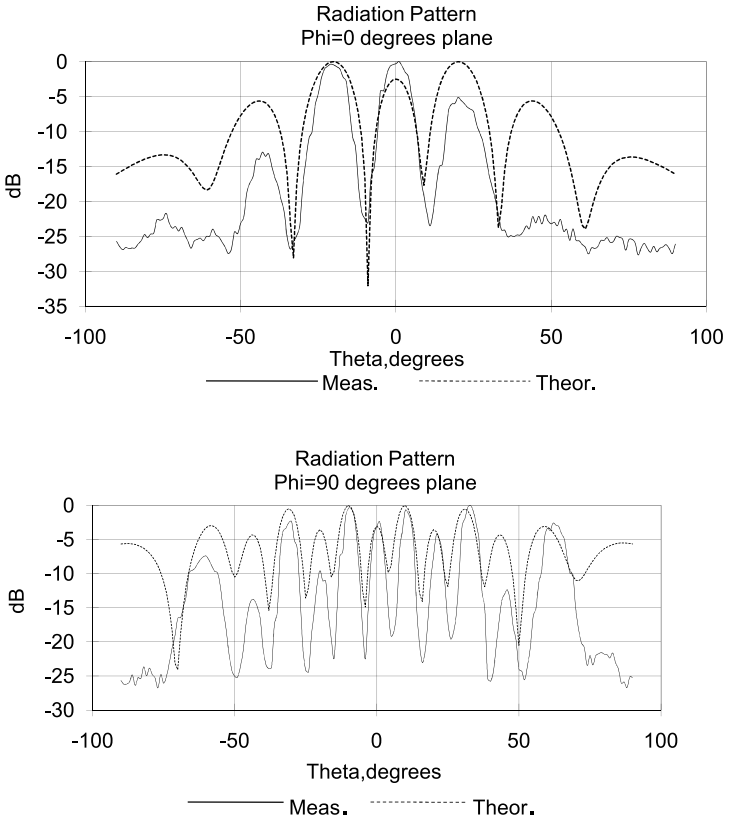

(b)

Figure 9. (a) Main lobe level for five-element Close planar array, (b) radiation pattern of five-element Close array ($R = 16.75$ cm), (c) radiation pattern of five-element Close array ($R = \infty$), (d) radiation pattern of five-element Close array ($R = -16.75$ cm). (color figure available online) (*continued*)

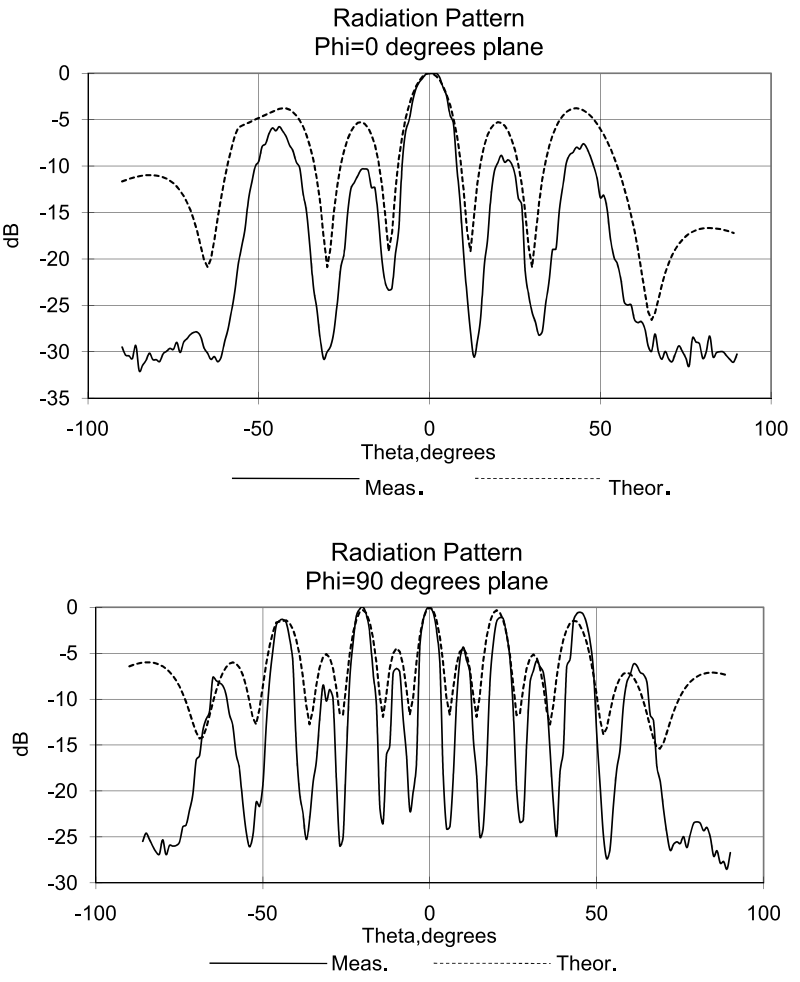

(c)

Figure 9. (*Continued*).

These figures show that the beam formation is more undulating in the $\phi = 90°$ plane than in the $\phi = 0°$ plane, which is predominantly decaying. In the $\phi = 90°$ plane, the peaks alternate in strength from high to low for all three conformal shapes of $R = \pm 16.75$ cm and planar. A potential application of this feature and for all other geometries is summarized Section 5.

In the $\phi = 0°$ polarization plane (Figures 9(b)–9(d), upper figures) the main lobe beam width varies from about 2°–5.5° and is greatest in planar regions, and the beam narrows in the spherical conformal cases ($R = \pm 16.75$ cm). Similarly, the first side lobe has its highest level in the planar geometry case and its intensity decreases for spherical geometries.

In the $\phi = 90°$ plane, the 3-dB beam width of the main lobe is smaller than in the $\phi = 0°$ plane; however, there is one interesting feature of the patterns in the $\phi = 90°$ plane—the multi-beam pattern is more widely separated compared to the patterns in the

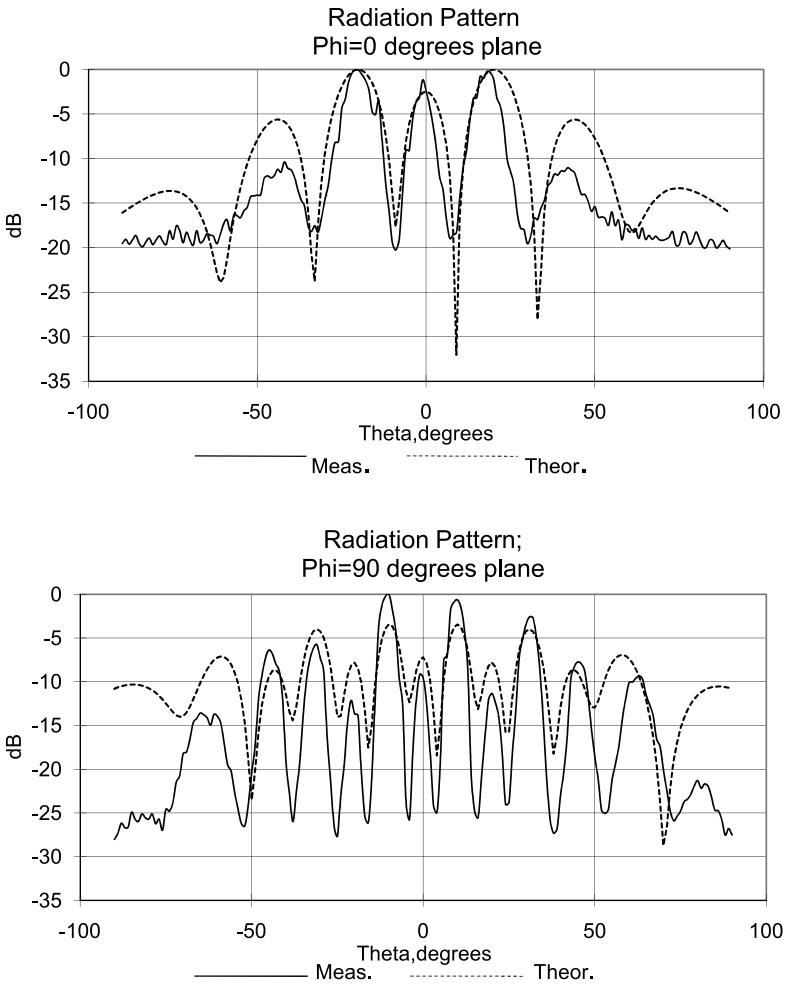

(d)

Figure 9. (*Continued*).

$\phi = 0°$ plane. High peaks are interspersed with low peaks, which could find potential application in satellite coverage of widely separated geographical areas.

4.4. Five-Element Far Planar Array

Finally, this section discusses measurement and simulation data for the last array configuration in this study for the Far geometry (Figure 4(d)) for sphere radii of 16.75 cm, ∞ (planar array), and -16.75 cm radii. The x-y-z coordinates of the array element positions are given in Table 5.

The measured and theoretical radiation pattern data are presented in Figures 10(a) through 10(d) for vertical array radii of $R = 16.75$ cm, $R = \infty$ (planar geometry), and $R = -16.75$ cm, respectively. Figure 10(a) compares the theoretical and measured

Table 5
Position coordinates of five-element array with Far geometry

Element number	x Position (cm)	y Position (cm)	z Position (cm) for $R = 16.75$ cm	z Position (cm) for planar	z Position (cm) for $R = -16.75$ cm
1	0	10.4	0	0	0
2	−5.1	0	−2.8	0	2.8
3	0	0	−3.6	0	3.6
4	5.1	0	−2.8	0	2.8
5	0	−10.4	0	0	0

gain variation with array radii in the $\phi = 0°$ plane, while Figures 10(b) through 10(d) compare the measured and theoretical radiation field patterns in both principal planes.

These figures show that multi-beam formation is exhibited in both the principal planes. However, the peak values show more variation in the $\phi = 90°$ plane than in the $\phi = 0°$ plane, where the peaks decay gradually. In the case of the $\phi = 0°$ polarization angle, the main lobe 3-dB beam width remains constant at around 3° for the planar geometries; however, the main beam is absent in both positive and negative spherical geometries.

In the $\phi = 90°$ polarization angle also, no real main beam existed at spherical geometries of $R = \pm 16.75$ cm. The main lobe 3-dB beam width for the planar array was narrower at around 1.5°, as compared with the $\phi = 0°$ polarization plane. In general, measurement data, including first side lobe and second side lobe levels, match well with simulation data.

Additionally, for the Far geometry (Figure 4d), an important observation can be made for spherical conformal geometries of $R = \pm 16.75$ cm; for both polarization angles of $\phi = 0°$ and $\phi = 90°$, there appears to be little or no main lobe compared to the planar geometry.

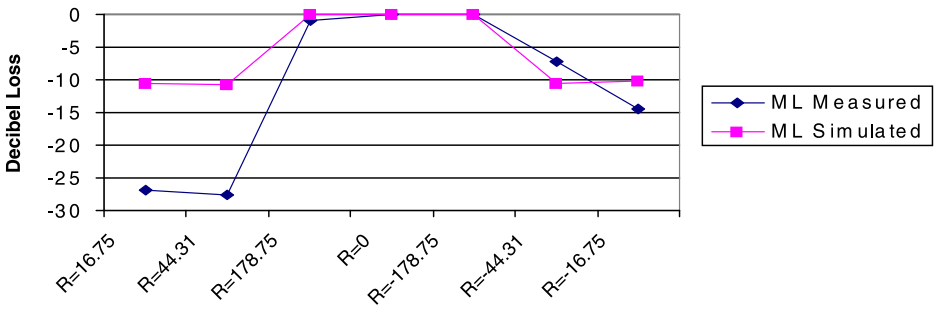

(a)

Figure 10. (a) Main lobe level for Far geometry at 16.769 GHz, (b) radiation pattern of five-element Far array ($R = 16.75$ cm), (c) radiation pattern of five-element Far array ($R = \infty$), and (d) radiation pattern of five-element Far array ($R = -16.75$ cm). (*continued*)

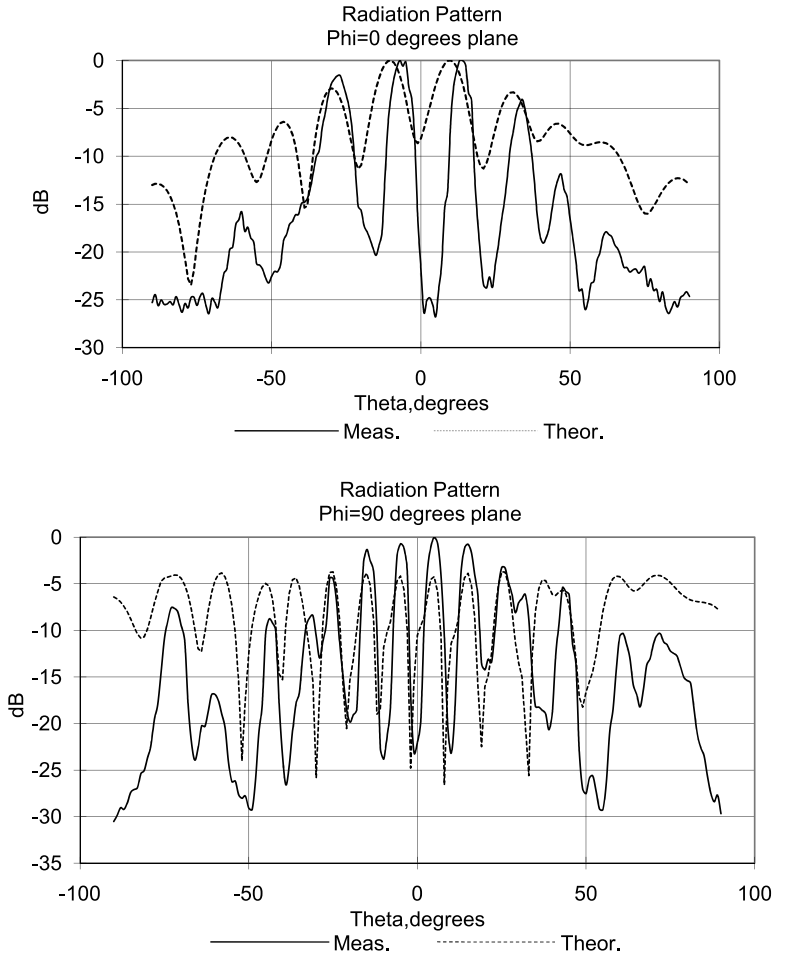

(b)

Figure 10. (*Continued*).

5. Summary and Conclusions

This article has presented the design, fabrication, simulation, and experimental characterization of a 16-GHz rectangular waveguide array that can be switched among different linear and planar configurations to generate single-beam or multi-beam patterns. Additionally, the geometry of the array can be shifted between planar and spherical profiles to control the individual beam properties. The geometry and application of these different array configurations are summarized in Table 6.

In all of the array configurations, it is observed that main properties, such as beamwdith and muti-beam properties, can be controlled by either switching the array from linear to planar modes or by adjusting the lateral movement of the central focusing element. The linear mode (vertical and horizontal) geometries generate a broad central beam in one principal plane of the array and narrow multiple beams in the orthogonal plane.

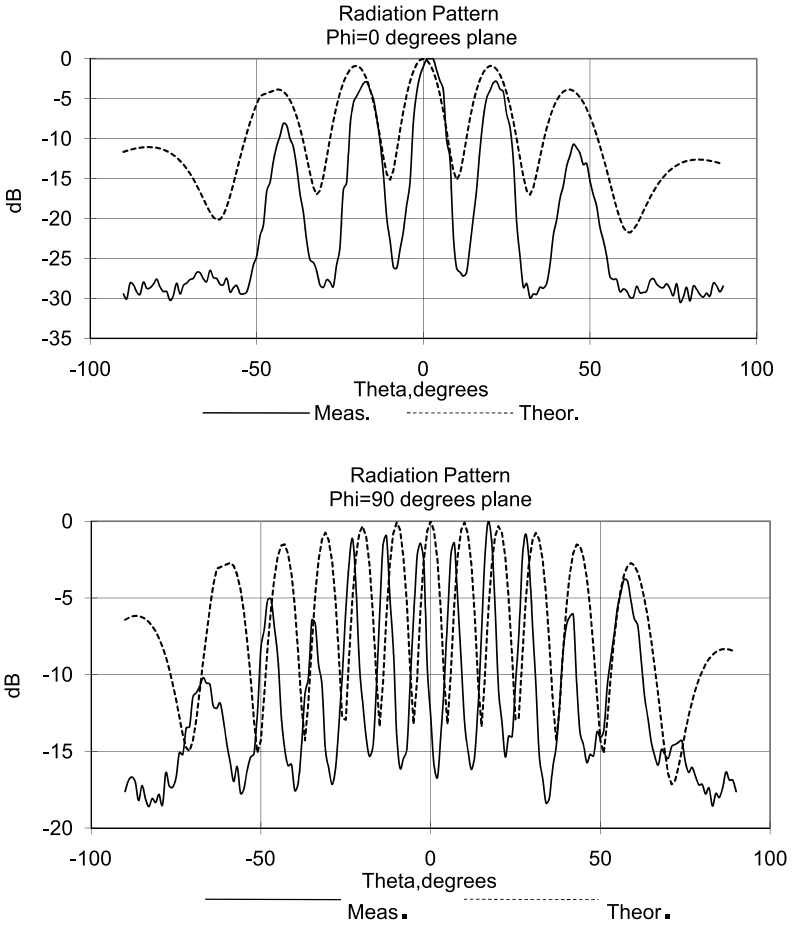

(c)

Figure 10. (*Continued*).

Table 6
Measured performance summary of different array configurations

Array geometry	Number of array elements	Array type	Radiation field properties		Possible satellite application
			$\phi = 0°$ plane	$\phi = 90°$ plane	
x-Axis	3	Linear	Multi-beam, narrow beam width, 2°–3°	Single beam, broad beam width, 18°–26°	Single coverage area in $\phi = 90°$ plane, multiple adjacent coverage areas in $\phi = 0°$ plane
y-Axis	3	Linear	Single beam, broad beam width, 18°–33°	Multi-beam, narrow beam width, ∼1°	Single coverage area in $\phi = 0°$ plane, multiple adjacent coverage areas in $\phi = 90°$ plane

(*continued*)

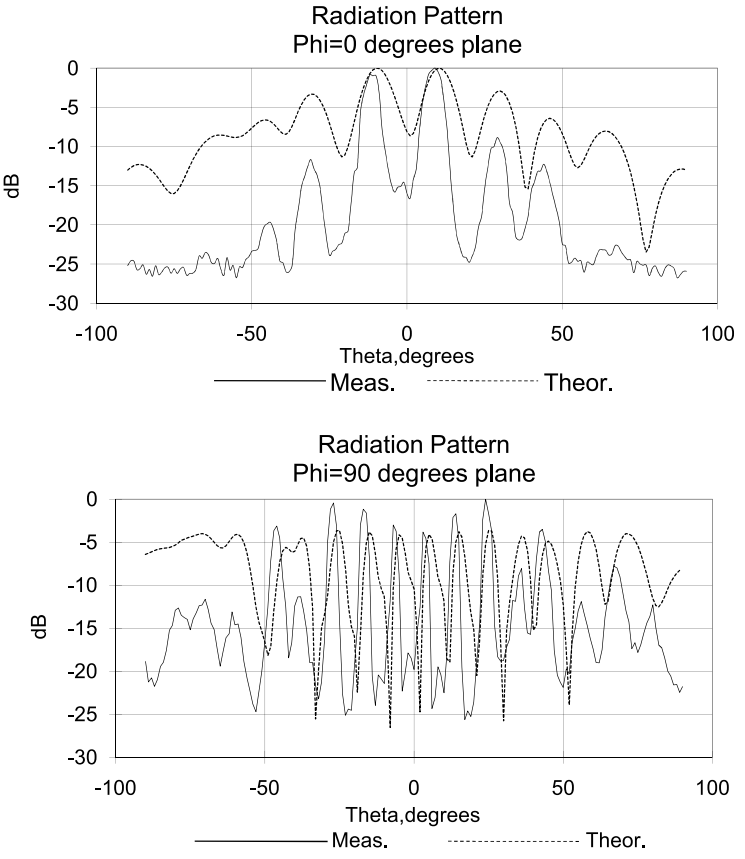

(d)

Figure 10. (*Continued*).

Table 6
(*Continued*)

Array geometry	Number of array elements	Array type	Radiation field properties		Possible satellite application
			$\phi = 0°$ plane	$\phi = 90°$ plane	
Close	5	Planar	Multi-beam, broad beam width, 2°–5°	Multi-beam, narrow beam width, 1°–2°	Multiple coverage areas in both $\phi = 0°$ and $\phi = 90°$ planes (with alternating high and low peaks)
Far	5	Planar	Multi-beam, broad beam width, ∼3°	Multi-beam, narrow beam width, ∼1.5°	Multiple coverage areas in both $\phi = 0°$ and $\phi = 90°$ planes (with relatively constant peaks)

In contrast, the planar mode (Close, Figure 4(c); and Far, Figure 4(d)) geometries generate narrow multiple beams in both principal planes of the array. However, while the Close planar array provides wide angular spacing between adjacent beams, the Far planar array provides narrow angular spacing. A consistent trend that is noticed in all array geometries is that the overall radiation patterns in both principal planes decay more rapidly in nonplanar geometries rather than in planar geometry.

Overall, it is seen that the different configurations of the array provide versatile properties, such as multi-beam formation and beamwidth control; however, a transition from planar to nonplanar geometry does not degrade pattern characteristics, such as maximum gain and side-lobe level. This is important in satellite systems, where the array has to perform multiple functions while maintaining acceptable signal quality.

Acknowledgment

The authors would like to thank the reviewers for their valuable suggestions to improve the quality of the article.

References

Balanis, C. A. 1997. *Antenna theory: Analysis and design*. New York: Wiley.

Bocquet, B., J. C. Van De Velde, A. Mamouni, Y. Leroy, G. Giaux, J. Delannoy, & D. Delvalee. 1990. Microwave radiometric imaging at 3 GHz for the exploration of breast tumors. *IEEE Trans. Microw. Theory Techniq.* 38:791–793.

Caille, G., E. Vourch, M. J. Martin, J. R. Mosig, & M. Polegre. 2002. Conformal array antenna for observation platforms in low Earth orbit. *IEEE Antennas Propagat. Mag.* 44:103–104.

Godara, L. C. 1997. Applications of antenna arrays to mobile communications, part I: Performance improvement, feasibility, and system considerations. *Proc. IEEE* 85:1031–1056.

Hansen, R. C. 1998. *Phased array antennas*. New Jersey: John Wiley.

Hopkins, G. D., D. L. Sherman, K. P. Pullen, & R. Zagrodnick. 2004. A K-band microstrip phased array radiator for airborne antennas. *Proc. 2004 IEEE Aerospace Conf.* 2:897–904.

Kumar, B. P., & G. R. Branner. 1994. The far-field of a spherical array of point dipoles. *IEEE Trans. Antennas Propagat.* 42:473–476.

Kumar, B. P., & G. R. Branner. 2005. Generalized technique for the synthesis of conformal antenna arrays with planar, cylindrical and spherical geometry. *IEEE Trans. Antennas Propagat.* 53:621–634.

Miyata, K. 1996. A 12 GHz-band planar waveguide array antenna for compact range application—a preliminary study. *IEEE Trans. Antennas Propagat.* 44:588–589.

Morton, T. E., & K. M. Pasala. 2006. Performance analysis of conformal conical arrays for airborne vehicles. *IEEE Trans. Aerospace Electron. Syst.* 42:876–890.

Pozar, D. M. 1990. *Microwave engineering*, 141–153, 716. Boston, MA: Addison-Wesley Publishing Company.

Sehm, T., A. Lehto, & A. V. Raisanen. 1998. A large planar 39-GHz antenna array of waveguide-fed horns. *IEEE Trans. Antennas Propagat.* 46:1189–1192.

Sterzer, F. 2002. Microwave medical devices. *IEEE Microw. Mag.* 3:65–70.

Valerie, P., R. Jackson, E. Hendrick, S. A. Feig, & D. B. Kopans. 1993. Imaging of the radiographically dense breast. *Radiology* 188:297–300.